

1 **Characteristics of airborne black carbon-containing particles**
2 **during the 2021 summer COVID-19 lockdown in a typical**
3 **Yangtze River Delta city, China**

4
5 Yuan Dai^{1,2,3}, Junfeng Wang^{1,2}, Houjun Wang³, Shijie Cui^{1,2}, Yunjiang Zhang^{1,2},
6 Haiwei Li^{1,2}, Yun Wu^{1,2}, Ming Wang^{1,2}, Eleonora Aruffo⁵, Xinlei Ge^{1,2,4*}

7
8 ¹Jiangsu Key Laboratory of Atmospheric Environment Monitoring and Pollution
9 Control, Collaborative Innovation Center of Atmospheric Environment and Equipment
10 Technology, School of Environmental Science and Engineering, Nanjing University of
11 Information Science and Technology, Nanjing 210044, China

12 ²International Joint Laboratory on Climate and Environment Change (ILCEC), Nanjing
13 University of Information Science and Technology, 210044 Nanjing, China

14 ³Yangzhou Environmental Monitoring Center, Yangzhou 225009, China

15 ⁴School of Environment and Energy Engineering, Anhui Jianzhu University, Hefei
16 230601, China

17 ⁵Department of Advanced Technologies in Medicine & Dentistry, University “G.
18 d’Annunzio” of Chieti-Pescara; Center for Advanced Studies and Technology-CAST,
19 Chieti 66100, Italy

20
21 **Correspondence:** Xinlei Ge (caxinra@163.com)

22 **Abstract**

23 Black carbon-containing particles (BCc) are ubiquitous in ambient air, significantly
24 contributing to particulate matter (PM) pollution. The unexpected outbreak of the
25 COVID-19 pandemic in the summer of 2021 prompted a localized and prolonged
26 lockdown in Yangzhou City, situated in the Yangtze River Delta, China. This lockdown
27 led to significantly altering in local anthropogenic emissions, while neighboring cities
28 continued regular operations, providing a unique opportunity for the investigation of
29 BCc characteristics influenced by varying emission conditions. Single particle aerosol
30 mass spectrometer (SPA-MS) analysis revealed a notable decrease in the proportion of
31 freshly emitted BCc during the lockdown period (LD). However, PM_{2.5} concentrations
32 remained relatively unchanged, with an observed increase in the proportion of aged
33 BCc during LD compared to the period before the lockdown (BLD). The study also
34 underscored the significant role of regional transport in PM_{2.5} pollution during the
35 campaign. Moreover, reactive trace gases (e.g., NO_x, SO₂, and VOCs) could form thick
36 coatings on pre-existing particles likely via enhanced heterogeneous hydrolysis under
37 high relative humidity (RH) as well, resulting in significant BCc particle growth (~600
38 nm), as well as PM_{2.5}, during LD. Our study highlights that short-term, strict local
39 emission controls may not effectively reduce PM pollution due to the complex
40 production and transmission characteristics of BCc and the non-linear responses of
41 PM_{2.5} to its precursors. Achieving further effective PM_{2.5} reduction mandates a focus
42 on nuanced control of BCc and necessitates a comprehensive and extensive approach
43 with a regionally coordinated and balanced control strategy through joint regulation.

44 **1. Introduction**

45 China has implemented long-term clean air measures to cut down anthropogenic
46 emissions and improve air quality (Ge et al., 2020), resulting in a nationwide reduction
47 of average fine particulate matter (PM_{2.5}, aerodynamic diameter $\leq 2.5 \mu\text{m}$) level from
48 $50 \mu\text{g m}^{-3}$ in 2015 to $30 \mu\text{g m}^{-3}$ in 2020 (Zhou et al., 2022). However, this PM_{2.5}
49 concentration remains significantly higher than the new World Health Organization
50 (WHO) guideline value of $5 \mu\text{g m}^{-3}$ (WHO Global Air Quality Guidelines, 2021). Black
51 carbon (BC) is a ubiquitous component of aerosols, typically constituting a small
52 proportion (5~10%) of PM_{2.5} in the atmosphere (Chen et al., 2020). However, freshly
53 emitted BC evolves into BC-containing particles (BCc) by undergoing atmospheric
54 aging, contributing to a rise in the total mass of PM_{2.5} through processes of coating or
55 embedding by other materials (Bond and Bergstrom, 2006; Peng et al., 2016). The
56 number and mass fraction of BCc can exceed 60% and 50% of PM_{2.5}, respectively,
57 emphasizing the significant role of BC in elevating the mass concentration of
58 particulate matter (PM) (Sun et al., 2022; Xie et al., 2020; Chen et al., 2020).

59
60 The atmospheric aging of BCc involves intricate chemical and physical transformations
61 that influence their mixing state, morphology, hygroscopicity, and optical properties,
62 all of which have profound implications for climate and human health (Bond et al.,
63 2013; Ramanathan et al., 2008). For example, freshly emitted BC particles are initially
64 hydrophobic but possess a porous surface structure that facilitates the internal or
65 external mixing with co-emitted primary organic/inorganic and secondary materials
66 that are associated with BC (Cheng et al., 2012; Li et al., 2020). On the other hand, BCc
67 undergoes continually aging processes, including the condensation of low-volatility
68 vapors (Li et al., 2022), coagulation with preexisting aerosols (Kondo et al., 2011), and
69 heterogeneous oxidation with gaseous pollutants (Zhang et al., 2024). This alteration
70 may affect the coating thickness, morphology, size distribution, and hygroscopicity of
71 BCc, thereby impacting their climate forcing as well as atmospheric lifetime (Luo et al.,
72 2022; Taylor et al., 2014). High loading of atmospheric BCc could also depress the
73 development of the planetary boundary layer and exacerbate PM pollution episodes
74 (Huang et al., 2018). BCc characteristics are influenced by various combustion sources
75 and emission conditions, including local industrial burning, vehicle exhausts,
76 residential coal burning, and biomass burning (Li et al., 2020; Sedlacek et al., 2022;
77 Zhang et al., 2018), as well as long-range transport from other regions (Adachi et al.,
78 2014; Zhang et al., 2021). Those diverse conditions complicate the development of
79 parameterizations of BCc properties, the insufficient understanding of complex
80 emission sources, aging processes, and physical properties of BCc, hampering the
81 effectiveness of air quality remediation (Cappa et al., 2019; Kahnert, 2010; Sun et al.,
82 2021).

83
84 Studies on the effects of large-scale and short-term stringent emission control events on
85 air quality in China have been widely deployed, e.g., the 2008 Beijing Olympic Games

86 (Wang et al., 2010; Zhou et al., 2010), the 2015 Asia-Pacific Economic Cooperation
87 (APEC) (Zhu et al., 2015), the 2014 Nanjing Youth Olympic Games (Wang et al., 2022)
88 and the national COVID-19 lockdown in 2020 winter (Huang et al., 2021; Le et al.,
89 2020; L. Li et al., 2020; Wang et al., 2020). Previous studies extensively investigated
90 air pollutant variations during the COVID-19 lockdown in the winter of 2020 across
91 different regions of the world. Stringent restrictions on industrial and vehicular
92 activities have resulted in significant reductions in gaseous pollutants and particulate
93 matter, not only in megacities (Chen et al., 2020; Jeong et al., 2022; Sun et al., 2020)
94 but also in middle-sized cities (Clemente et al., 2022; Wang et al., 2021; Xu et al., 2020)
95 and rural areas (Cui et al., 2021, 2020; Jain et al., 2021). Compared to the decreasing
96 trends observed in most cities worldwide, the level of PM_{2.5} in Shanghai (Chang et al.,
97 2020), Hohhot (Zhou et al., 2022), and the Northeast of China Plain (Nie et al., 2021)
98 increased unexpectedly. These observations reveal the complex aerosol chemistry of
99 PM_{2.5} comprising primary and secondary components. The reduction of primary
100 pollutants during lockdown resulted in a shift towards a higher proportion of secondary
101 aerosols, including inorganic and organic species, exhibiting a non-linear response to
102 emission changes (Zhang et al., 2021). Furthermore, some studies suggested that the
103 increase in secondary aerosols during lockdown is due to the enhanced atmospheric
104 oxidative capacity resulting from the rise in ozone levels (Wang et al., 2021),
105 unfavorable meteorological conditions (Chien et al., 2022; Sulaymon et al., 2021a),
106 changes of local and regional emission sources (Feng et al., 2022). However, most
107 previous studies focused on lockdown events during the cold seasons, and studies on
108 summer lockdown events in China were very limited.

109
110 Yangzhou is located in the central region of the Yangtze River Delta (YRD), at the
111 junction of the Yangtze River and, the Beijing-Hangzhou Grand Canal, which serves as
112 a prominent economic city, industrial-intensive area, and highly active inland shipping
113 node in East China. Due to the complex emissions and feedback with the East Asian
114 monsoons (Ding et al., 2019), this region is susceptible to anthropogenic aerosols,
115 especially BC_c originating from chemical, steelmaking, coal-fired, petrochemical
116 enterprises, and transportation, etc. Extensive studies have investigated the responses
117 of atmospheric pollutants to emission changes during the COVID-19 lockdown
118 measures in the YRD (Chen et al., 2021; Li et al., 2020; Qin et al., 2021; Zhang et al.,
119 2022). However, the key chemical and physical processes specifically responsible for
120 the BC_c in this region are still unclear. During the summer of 2021, Yangzhou
121 experienced a resurgence of COVID-19 with over 500 confirmed cases. In response,
122 stringent public health measures were imposed from July 29th to September 10th,
123 including the closure of public transport, and suspension of non-essential industrial
124 plants, restaurants, shopping malls, and entertainment clubs. People were also
125 mandated to quarantine at home. Consequently, Yangzhou experienced a significant
126 decline in transportation and industrial energy consumption, dropping by nearly 46%
127 and 25%, respectively, compared to the same period in 2020 (www.yangzhou.gov.cn),

128 implying a substantial reduction in human activity and primary emissions. Unlike the
129 nationwide COVID-19 lockdown in China during the cold season of 2020 (Le et al.,
130 2020; Sulaymon et al., 2021b), the summer lockdown in Yangzhou was more localized
131 but protracted, significantly altering local anthropogenic emissions while neighboring
132 cities maintained regular operations, which provides a unique opportunity to explore
133 and compare the diverse mixing states and, the aging process of BCc in different
134 anthropogenic emission conditions in summer. Here we report the chemical
135 compositions and aging characteristics of airborne BCc in YRD. Our investigation
136 involved a combination of ground measurements, spaceborne observations, and mass
137 spectrometric analysis conducted during the COVID-19 lockdown in the summer of
138 2021 in Yangzhou. Additionally, we employed potential source contribution function
139 (PSCF) analysis to investigate the air pollution patterns in the YRD.

140

141 **2. Methods**

142 **2.1 Sampling site and instruments**

143 The in-situ online measurements were conducted at a rooftop laboratory 20 m above
144 ground located in a national air quality monitoring station, Yangzhou Environmental
145 Monitoring Center (32.41°N, 119.40°E), Yangzhou, China (**Figure 1**). This sampling
146 site is a typical urban site surrounded by residential areas, arterial roads, parks,
147 restaurants, and shopping centers. In this study, the measurement period was divided
148 into three phases: the before-lockdown period (BLD: 30 June to 28 July 2021), the
149 lockdown period (LD: 29 July to 9 September 2021), and the after-lockdown period
150 (ALD: 10 September to 7 October 2021) (**Figure 2**).

151

152 A single-particle aerosol mass spectrometer (SPA-MS, Hexin Analytical Instrument Co.,
153 Ltd., China) was deployed during the field campaign to obtain the chemical
154 composition, size distribution, and mixing state of individual PM_{2.5} particles. A cyclone
155 with a 2.5 μm cutpoint (Model URG-2000-30ED) and a Nafion dryer is equipped in
156 front of the sampling inlet. Individual particles are introduced into the SPA-MS through
157 a critical orifice at a flow rate of 3 L min⁻¹. The vacuum aerodynamic diameters (D_{va})
158 are determined using the velocities derived from two continuous laser beams (diode Nd:
159 YAG, 532 nm) spaced 6 cm apart. Subsequently, these particles are desorbed and
160 ionized by a downstream pulsed laser (266 nm), and ion fragments are generated and
161 measured by a Z-shaped bipolar time-of-flight mass spectrometer. A more detailed
162 description of SPA-MS can be found in previous studies (Li et al., 2011).

163

164 PM_{2.5} mass concentration was measured by a particulate matter monitor (XHPM2000E,
165 Xianhe, China). Nitrogen oxides (NO_x = NO + NO₂), SO₂, and ozone (O₃)
166 concentrations were detected with a set of Thermo Fisher Scientific instruments
167 (Models 42i, 43i, and 49i). The concentrations of 103 volatile organic compounds
168 (VOCs) in ambient air, comprising 57 ozone precursors (PAMS), 12 aldehydes and
169 ketones, and 34 toxic organics (TO15), were continuously monitored at hourly intervals

170 using an online device (TH-300B, Tianhong, China). Meteorological parameters,
171 including ambient temperature (T), relative humidity (RH), wind direction (WD), and
172 wind speed (WS) were observed synchronously using an automatic weather instrument
173 (WXT530, Vaisala, Finland). Precipitation (PCP) data was obtained from the Yangzhou
174 Meteorological Bureau. All online data presented in this paper were hourly averaged at
175 local time (Beijing time, UTC+8).

176

177 2.2 Data analysis

178 2.2.1 Satellite Product

179 In this study, we utilized the Copernicus Atmosphere Monitoring Service (CAMS)
180 Global Near-Real-Time dataset (available at [https://developers.google.com/earth-](https://developers.google.com/earth-engine/datasets/catalog/ECMWF_CAMS_NRT)
181 [engine/datasets/catalog/ECMWF_CAMS_NRT](https://developers.google.com/earth-engine/datasets/catalog/ECMWF_CAMS_NRT)), acquired from the European Centre
182 for Medium-Range Weather Forecasts (ECMWF), to analyze the distribution of total
183 surface column concentrations of NO₂, SO₂ and surface PM_{2.5} mass concentration.
184 CAMS offers the capacity to continuously monitor the composition of the Earth's
185 atmosphere at global and regional scales since 2016, with a spatial resolution of 44528
186 meters (Benedetti et al., 2009; Morcrette et al., 2009). The details of the bands of the
187 dataset used in this study are shown in Table S2. We calculated and plotted the averaged
188 2-dimensional data of ECMWF/CAMS/NRT NO₂, SO₂, and PM_{2.5} during BLD and LD
189 over the region of interest (17.93~54.74 °N, 71.21~142.23 °E) using Google Earth
190 Engine (Gorelick et al., 2017). The integration of remote sensing measurements has
191 provided a more comprehensive understanding of the sources and distributions of
192 particle matter and gaseous pollutants facilitating the evaluation of the impact of human
193 activities on air quality.

194 2.2.2 Geographic Source Analysis

195 The potential source contribution function (PSCF) analysis, based on the Hybrid
196 Single-Particle Lagrangian Integrated Trajectory (HYSPLIT) model, can be employed
197 to identify regional sources of air pollutants. Before conducting the PSCF analysis, 36
198 hours of air mass backward trajectories with one-hour resolution at 500 m above ground
199 level were calculated using the wind data from the Global Data Assimilation System
200 (GDAS) provided by the National Oceanic and Atmospheric Administration (NOAA)
201 (Wang et al., 2009). An open-source software MeteoInfo (Wang, 2014) was utilized for
202 the PSCF analysis. The whole study area (110.1~133.4 °E and 21.3~39.9 °N) covered
203 by the trajectories was divided into thousands of cells with a spatial resolution of 0.1°
204 × 0.1°. The PSCF was simulated according to the following equation:

$$205 \quad PSCF_{ij} = \frac{m_{ij}}{n_{ij}} \quad (1)$$

206 where $PSCF_{ij}$ is the conditional probability that the grid cell (i, j) was a source of the
207 species found in high concentration (Hopke et al., 1993); n_{ij} is the number of all
208 trajectories passing through this grid cell, and m_{ij} is the number of trajectories. In this
209 study, the pollution criterion values for different BCc particle types were set as the 75th

210 percentile of hourly average number fractions, respectively. To further improve the
 211 accuracy of the PSCF analysis and minimize analytical uncertainties, the Weighted
 212 PSCF (WPSCF) functions as shown in Equation (2~3) were applied (Polissar et al.,
 213 1999). The weight (W_{ij}) for each grid cell was determined based on the number of
 214 trajectory endpoints (n_{ij}) as follows:

$$215 \quad WPSCF_{ij} = W_{ij} \times PSCF_{ij} \quad (2)$$

$$216 \quad W_{ij} = \begin{cases} 1.00 & n_{ij} > 3n_{ave} \\ 0.70 & 1.5n_{ave} < n_{ij} \leq 3n_{ave} \\ 0.40 & n_{ave} < n_{ij} \leq 1.5n_{ave} \\ 0.17 & n_{ij} \leq n_{ave} \end{cases} \quad (3)$$

217 Here, n_{ave} is the average number of trajectory endpoints of each grid.

218 2.2.3 SPA-MS Data Analysis

219 In total, 1649574 particles were analyzed during the entire observation period. The size
 220 and chemical composition of single particles were analyzed using the Computational
 221 Continuation Core (COCO V1.4) toolkit in MATLAB 2022 (The MathWorks, Inc.).
 222 Our focus was on BCc, which was identified based on the relative peak area (RPA) of
 223 carbon ion clusters (C_n^+ , $n = 1, 2, 3, \dots$), with a threshold of 0.05 (Zhang et al., 2021).
 224 An adaptive resonance theory-based neural network algorithm (ART-2a) was applied
 225 to classify the measured individual particles based on the presence and intensity of ion
 226 peaks, with a vigilance factor of 0.75, a learning rate of 0.05, and 20 iterations (Song et
 227 al., 1999).

228

229 3. Results and discussion

230 3.1 Field observations

231 **Figure 2** presents the temporal variations of meteorological parameters, $PM_{2.5}$, NO_x ,
 232 and SO_2 concentrations. Notably, significantly reductions in $PM_{2.5}$, NO_x , and SO_2 were
 233 observed at the end of BLD due to a high precipitation event, with a peak hourly
 234 precipitation reaching 37 mm, and the data collected during this event were excluded
 235 from the analysis. During BLD, the mean temperature (T) was 28 ± 3 °C, the total
 236 precipitation was 221 mm, with an average relative humidity (RH) of $83 \pm 12\%$. The
 237 prevailing winds originated from the south and southeast, with a mean wind speed (WS)
 238 of 3.3 ± 1.2 m s^{-1} . In comparison, LD shows a decline in temperature to 27 ± 2 °C and WS
 239 to 2.3 ± 1.0 m s^{-1} , but an increase in RH to $87 \pm 11\%$ and a reduction in total precipitation
 240 to 86 mm. **Figure S2b and c** present uniform distributions of RH and boundary-layer
 241 height (BLH) across the YRD during LD. These regional meteorological conditions and
 242 the effective removal of the pollutants accumulated at the end of BLD facilitated the
 243 investigation of BCc regional transport in YRD. During ALD, the temperature declined
 244 further to 25 ± 3 °C, WS increased to 3.3 ± 1.5 m s^{-1} , and total precipitation dropped to 27
 245 mm with a lower RH of $77 \pm 14\%$.

246

247 During LD, strict measures resulted in notably lower surface concentrations of PM_{2.5}
248 (20.3 μg m⁻³), NO_x (16.8 μg m⁻³) and TVOC (55.9 μg m⁻³) compared to BLD and ALD.
249 Conversely, the surface O₃ concentration showed an increase of 18.4 μg m⁻³ (28%)
250 during LD relative to BLD. The reduction of fresh NO emission alleviates O₃ titration
251 (Steinfeld, 1998) could be an explanation. Analysis from **Figure S3** indicates that the
252 O₃ level is higher than those of neighboring cities in the YRD, suggesting higher local
253 atmospheric oxidation capacity during LD. However, the average concentrations of
254 PM_{2.5} (20.6 vs. 20.3 μg m⁻³), SO₂ (9.1 vs. 9.2 μg m⁻³) and CO (0.61 vs. 0.62 mg m⁻³)
255 were comparable during both BLD and LD (**Figure 3**).

256
257 After LD, social activities gradually resumed in Yangzhou City, leading to an apparent
258 increase in all observed pollutants during the ALD period. For instance, there were
259 relative increases of 66% for NO_x, 19% for SO₂, 36% for TVOC, 14% for O₃, 32% for
260 PM_{2.5}, and 16% for CO from LD to ALD, respectively (**Figure 3**). **Given that both BC**
261 **and CO are byproducts of incomplete combustion of carbon-containing fuels (Wang et**
262 **al., 2015), and the high correlation between BC and CO (Zhou et al., 2009), it is**
263 **plausible to infer that the primary emission source of BC during LD differed from those**
264 **during ALD. This change likely reflects the shift in combustion practices and fuel usage**
265 **patterns as economic activities restarted during ALD.**

266
267 Satellite-retrieved PM_{2.5}, NO₂, and SO₂ data over the entire region of eastern China
268 were also investigated, and results show that these pollutants were predominantly
269 concentrated in Shanghai and its neighboring cities, including Yangzhou, during both
270 BLD and LD (**Figure S4**). **Figure 4** presents regional fractional changes of mean PM_{2.5},
271 NO₂, and SO₂ concentrations from the BLD to LD periods in YRD, all showing an
272 increase of 29%, 6%, and 14%, respectively. In comparison, Yangzhou city experienced
273 lower increases in these air pollutants, with slight changes of 6%, -18%, and -4% for
274 PM_{2.5}, NO₂, and SO₂, respectively. The implication is that, even though local primary
275 emissions, such as NO₂, and SO₂, were reduced substantially during LD, they still could
276 be affected by regional transport. Furthermore, as depicted in **Figure S3**, the
277 concentrations of NO₂ in major cities of the YRD were more than twice higher than in
278 Yangzhou during LD, confirming a relatively lower local primary emissions due to the
279 stringent lockdown. However, the higher level of SO₂ in Yangzhou during LD may be
280 attributed to the nearby power stations along the Yangtze River, which were not
281 impacted by the lockdown measures.

282 3.2 Chemical composition and size distribution of individual BCc

283 Based on the SPA-MS analysis, a total of 1068362 BCc was collected during the whole
284 study period. The BCc accounted for 59%, 69%, and 57% of the total number of
285 measured particles in the BLD, LD, and ALD periods, respectively. **Figure 5** shows the
286 normalized average mass spectra of BCc during three periods. Ion height in each
287 spectrum reflects the number fraction of the detected BCc with the corresponding ion
288

带格式的: 非删除线

带格式的: 非删除线

带格式的: 非删除线

带格式的: 非删除线

带格式的: 非删除线

带格式的: 非删除线, 突出显示

带格式的: 非删除线

289 to the total BCc, while colors represent peak area ranges of detected ions. BCc in BLD,
290 LD, and ALD shown similar mass spectra at $m/z < 100$, with common peaks including
291 carbon ion clusters (C_n^+ , $n = 1\sim7$), m/z 27[$C_2H_3^+$], 37[C_3H^+], 43[$C_2H_3O^+$], 51[$C_4H_3^+$],
292 63[$C_5H_3^+$], 46[NO_2^-], 62[NO_3^-], and 97[HSO_4^-]. However, the abundance of large m/z
293 carbon ions (C_n^+ , $n > 7$) in both BLD and ALD periods was 1.5 times higher than that in
294 the LD. Previous studies have indicated that high-mass carbon ions may be linked to
295 traffic emissions, particularly those from diesel trucks (Xie et al., 2020; Liu et al., 2019),
296 and the observed reduction in such ions during LD suggests a decrease in local vehicle
297 emissions. This trend is also consistent with the changes observed in aromatic
298 compounds, e.g. m/z 119[$C_9H_{11}^+$].

299
300 Further, BCc was classified into 12 types based on the differences in chemical features
301 and temporal variations, as shown in **Table S1**. Fresh BC particles (BC-fresh) are those
302 freshly emitted without undergoing significant atmospheric processing (Ding et al.,
303 2021). Five types of BC-fresh particles were identified according to their ion markers:
304 (i) BC-pure is dominated by carbon clusters (C_n^+) with minor ion signals of inorganic
305 species, such as m/z 46[NO_2^-] and m/z 97[HSO_4^-] from nitrate and sulfate, respectively
306 (Xie et al., 2020); (ii) BCc from biomass burning (BB) are characterized by ion signals
307 at m/z 39[K^+], 45[CHO_2^-], 59[$C_2H_3O_2^-$], and 73[$C_3H_5O_2^-$], with a relative peak area
308 (RPA) more than 0.5 (Silva et al., 1999); (iii) coal combustion BCc (CC) typically
309 include small carbon clusters (C_n^+ , $n = 1\sim4$), metal elements (e.g., m/z 7[Li^+], 23[Na^+],
310 27[Al^+], 56[Fe^+], 63[Cu^+] and 206/207/208[Pb^+]), and organic carbon (38[$C_3H_2^+$],
311 43[$C_2H_3O^+$]) peaks in the positive mass spectrum, while the strong signals of secondary
312 inorganic species (46[NO_2^-], 43[AlO^-], 62[NO_3^-], 80[SO_3^-], 97[HSO_4^-]) in the
313 negative ion mode suggest that CC particles were long-distance transported or more
314 processed (Zhang et al., 2022; Zhang et al., 2009); (iv) particles from vehicle emission
315 (VE) are characterized by the presence of ion signals at m/z 40[Ca^+], 51[V^+], 55[Mn^+],
316 67[VO^+], 46[NO_2^-], 62[NO_3^-], and 79[PO_3^-], as well as high loadings of organic carbon
317 (41[$C_3H_5^+$], 43[$C_2H_3O^+$]) and carbon clusters (C_n^+ , $n = 1\sim4$) ion peaks (Yang et al., 2017);
318 (v) BCc that are internally mixed with more than one type (BB, CC, and VE) are
319 categorized as Mix type (Sun et al., 2022).

320
321 Aged BC particles, denote as BC-aged, undergo a series of chemical reactions and
322 physical transformations. These processes typically lead to changes in their morphology,
323 hygroscopicity, and optical properties as they are coated with other materials (He et al.,
324 2015). Six types of BCc are classified as BC-aged and are further grouped into BCOC
325 and BC-SNA, depending on whether they contain mainly organic carbon (OC) or
326 sulfate/nitrate/ammonium (SNA). First, BCOC types indicate BC-aged particles that
327 are internally mixed with OC. These particles are characterized by the presence of
328 carbon clusters (C_n^+) and $C_nH_m^+$ ions ($n = 1\sim6$, $m = 1\sim3$) in positive mass spectra (Xie
329 et al., 2020). On the other hand, BC-aged particles that do not mix with OC are named
330 BC-SNA indicating the mix with secondary inorganic species. Additionally, BCOC

331 particles with negative mass spectra dominated by nitrate ions ($46[\text{NO}_2]^-$ and $62[\text{NO}_3]^-$)
332 or sulfate ions ($97[\text{HSO}_4]^-$) are referred to as BCOC-N or BCOC-S, respectively;
333 otherwise, BCOC particles showing similar peak areas of nitrate and sulfate are named
334 BCOC-SN. The BC-SNA particles are further categorized as BC-N, BC-S, and BC-SN
335 based on similar principles. Note the remaining particles that cannot be classified into
336 either BC-fresh or BC-aged ones are denoted as BC-other. More details of BCc particle
337 types are shown in **Table S1** and **Figure S1** in the Supplement.

338

339 During BLD, the average number fraction of BC-fresh particles was 36% with sizes
340 mainly concentrated at 500 nm, similar to the mode size of BC-aged particles was 520
341 nm (**Figures 6**). The predominant BCc types during BLD were BCOC-S and BC-S (24%
342 and 12% by number), likely because sulfate was removed less efficiently than organic
343 matter (OM) and NO_3 by heavy precipitation, especially during the warm seasons
344 (Isokääntä et al., 2022). As shown in **Figures 6c and d**, the peak size of BC-SNA was
345 larger than that of BCOC in all periods, indicating that organics coated BCc generally
346 had a relatively thin coating compared to those coated by secondary inorganic species,
347 which is consistent with previous studies (Sun et al., 2016; Wang et al., 2019).

348

349 During the transition from BLD to LD, heavy and continuous precipitation occurred
350 from July 25th to July 28th (the eve of lockdown), resulting in the removal of a majority
351 of the pollutants ($\text{PM}_{2.5}$: $4 \mu\text{g m}^{-3}$, O_3 : $35 \mu\text{g m}^{-3}$, NO_x : $8 \mu\text{g m}^{-3}$). Following this
352 environmental clearance, strict lockdown measures were implemented, resulting in a
353 drastic reduction in primary emissions. As a result, the number fraction of BC-fresh
354 particles significantly decreased from 37% to 28% and that of VE-type particles
355 dropped from 12% to 3% (by number). Expectedly, with the decrease in NO_x , an
356 obvious enhancement of O_3 was observed during LD (**Figure 3**). According to previous
357 studies (Huang et al., 2021; Laughner et al., 2021), large reduction of NO_x may promote
358 the formation of O_3 under a VOC-limited regime and enhance the oxidation capacity of
359 the local atmosphere, which may promote the number fraction of BC-aged particles
360 increased from 64% in the BLD to 72% in LD (**Figure 7a**), indicating the lockdown
361 could accelerate aging of BCc through complicated chemical reactions and/or physical
362 coagulation. Additionally, the most abundant type of BCc changed from BCOC-S (24%
363 by number) in the BLD to BC-N (25%) in LD (**Figure 7a**), suggesting different BCc
364 formation pathways. Despite the abrupt reductions of NO_x (-39%) due to the city
365 lockdown, it is important to note that the concentration of $\text{PM}_{2.5}$ only slightly decreased
366 during LD (-1%), highlighting the non-linear relationship between primary emissions
367 and $\text{PM}_{2.5}$ levels.

368

369 During ALD ($\text{PM}_{2.5}$: $26.7 \mu\text{g m}^{-3}$, NO_x : $27.9 \mu\text{g m}^{-3}$, TVOC: $76.0 \mu\text{g m}^{-3}$), the number
370 fraction of BC-fresh particles rose from 28% (LD) to 31% (ALD), while the fraction of
371 VE particles also increased from 3% (LD) to 12% (ALD) (**Figure 7a**), coinciding with
372 a 16% rise in CO concentration. This suggests a shift in combustion practices and fuel

373 usage patterns as economic activities resumed. The increased CO levels, a known
374 marker for combustion-related emissions, align with the resurgence of vehicle
375 emissions and other activities that emit BC and CO concurrently (Wang et al., 2015,
376 Zhou et al., 2009). Notably, the size distributions of BC-fresh and BC-aged particles
377 presented relatively small peaks at 690 nm and 820 nm during ALD, in addition to the
378 prominent peaks at 490 nm and 500 nm, which were different from those in the BLD
379 and LD periods. These small peaks were relatively close to the dominant sizes of BC-
380 fresh and BC-aged particles during LD (**Figure 6**). This result suggests that a substantial
381 number of BCc with small sizes (around 500 nm) after the lockdown was lifted in
382 Yangzhou, owing to the sudden enhancement of primary emissions; on the other hand,
383 particles with large diameters (>690 nm) may have formed due to the participation of
384 more trace reactive gases (e.g., NO_x, SO₂, and VOCs) in continuous aging reactions,
385 resulting in thicker coatings on the surface of pre-existing particles and therefore a more
386 clear separation of two-mode sizes during the ALD period than during the other two
387 periods. This hypothesis was also supported by the increased number fraction of
388 BCOC-SN during the ALD period (**Figure 7a**). Similar findings have been reported in
389 the North China Plain (NCP) and the YRD during cold seasons, where thicker coatings
390 on secondary aerosols were also observed under lower RH (<70%) (Zhang et al., 2021).
391 This might be due to that particles with more organics and nitrate can result in earlier
392 deliquescence and provide aqueous surfaces that facilitate the heterogeneous formation
393 of secondary species under relatively low RH (Zhang et al., 2021). Among the three
394 periods, the difference between the mode sizes of BC-aged and BC-fresh particles was
395 the smallest (10 nm) during the ALD period (**Figure 6a and b**). This size reduction can
396 be attributed to the increased BCOC and hydrophobic primary particles after lockdown
397 (Figure 7). Because the internally mixed BCOC and hydrophobic primary particles may
398 constrain further growth of secondary BC-SNA particles (Liu et al., 2016; Zhang et al.,
399 2018), thereby leading to smaller-sized BC-aged particles. Moreover, the differences in
400 BCc mode sizes between ALD and BLD periods also reveal an interesting fact that the
401 lockdown effect may not only affect air quality during lockdown but also can influence
402 the air quality even after lockdown, as the resumed emissions after lockdown may be
403 subjected to different chemistry from that before lockdown.

404
405 Throughout the entire observation, the changes in the number fraction of BC-SNA
406 exhibited consistency with the variations in RH (**Figure 7b**), indicating that BC tends
407 to mix with ammonium sulfate and ammonium nitrate under high RH conditions.
408 Meanwhile, the number fraction of BCOC shows similar patterns as TVOC, suggesting
409 that high TVOC levels may facilitate the coating of organics on BC cores under low
410 RH condition. **Figure 8** displays the number fraction of BCc species as a function of
411 PM_{2.5}. Overall, as PM_{2.5} levels increased, the number fraction of BC-aged particles also
412 increased, while the proportion of BC-fresh particles decreased during BLD and LD,
413 indicating a clear transition from BC-fresh particles to more aged ones, in line with the
414 average size distribution during ALD has a small peak at 900 nm. Specifically, the

415 increase in PM_{2.5} was driven by BCOC-S during BLD (**Figure 8a**), whereas BC-N
416 played a vital role in the PM_{2.5} increase during LD (**Figure 8b**). Interestingly, the
417 concentration of NO_x, the primary precursor of BC-N, decreased by 31% and 41%
418 during LD compared to BLD and ALD, respectively (**Figure 3**), indicating a strong
419 non-linear response of nitrate in BCc to NO_x, likely due to much faster conversion of
420 NO_x to nitrate upon enhanced atmospheric oxidation capacity; additionally, the high
421 proportion of BC-N during LD might be attributed to regional transport, similar to that
422 in Shanghai during 2020 winter lockdown (Chang et al., 2020).

423

424 3.3 Chemical aging of BCc

425 As shown in **Figure 5**, in the average positive mass spectra of total BCc, the peak areas
426 of C_n⁺, OM, and metals contributed to more than 95% of the total, while nitrate and
427 sulfate peak areas accounted for more than 90% of the negative mass spectral signal.
428 To better elucidate the aging processes of BCc during different lockdown periods, we
429 summed the carbon clusters C_n⁺ (n = 1~5, accounting for more than 99% of C_n) peak
430 areas to represent BC, and the total peak area of sulfate, nitrate, and ammonium (SNA)
431 to represent the second inorganic components coated on BC. Additionally, we defined
432 the sum of positive peak areas, excluding C_n⁺ and metals, as OC to represent the OM
433 coated on BC. These peak areas encompassed almost all the coating materials, except
434 for metals, of BCc. The changes in the mixing state and morphology of BCc can provide
435 insights into their aging characteristics, as reported previously (Kandler et al., 2018;
436 Moffet et al., 2013). In this study, we use OC/C_n and SNA/C_n ratios to describe different
437 types of chemical components coated on BC-fresh, and we use the ratio of the mode
438 size of BC-aged (D_{aged}) to that of contemporaneous BC-fresh (D_{fresh}) to represent the
439 aging degree of BCc.

440

441 **Figure 9** illustrates the diurnal variations of the OC/C_n and SNA/C_n ratios along with
442 the size distribution of BCc during different periods. We observed that both OC/C_n and
443 SNA/C_n increased during nighttime and decreased during daytime. These variations
444 showed the prominent enhancements of nocturnal OM and SNA, which could be
445 attributed to the accelerated gas-to-particle partitioning and nocturnal secondary
446 formation of organic/inorganic components under high relative humidity (RH > 85%)
447 and relatively stagnant air mass (WS < 3 m s⁻¹) (**Figure S5**). It is worth noting that from
448 BLD to LD and ALD, the intensity of diurnal variations of OC/C_n and SNA/C_n
449 increased obviously. This discrepancy can be attributed to several reasons. (i) During
450 BLD, the frequent precipitations effectively scavenged the particles (Isokääntä et al.,
451 2022); (ii) In contrast, stronger solar radiation and higher O₃ concentration during LD
452 promoted photochemical formations of OC and SNA; (iii) After lockdown, more
453 precursors due to increased local emissions may lead to more production of secondary
454 components than that during BLD as explained earlier. These results indicate that the
455 aging process and mixing state of BCc depend strongly on meteorological conditions
456 as well as emission sources in urban cities.

457

458 As shown in **Figure 9**, BCc with ~400 nm D_{va} exhibited significant diurnal fluctuations
459 in the OC/ C_n and SNA/ C_n ratios, during LD. There is a noticeable increase in the
460 proportion of BC-SNA particles during nighttime when RH is relatively high. These
461 observations suggest that nighttime heterogeneous hydrolysis may be considered a key
462 mechanism responsible for the formation of BCOC and BC-SNA particles. According
463 to Jacobson (2002), coagulation can be significant between particles with sizes <100nm
464 and >1 μ m but insignificant for particles of >300nm, when the total particle number
465 concentration is higher than 10^4 cm⁻³. During LD, the OC/ C_n and SNA/ C_n ratios of BCc
466 with ~400 nm D_{va} exhibited pronounced diurnal variations (**Figure 9**) and the number
467 fraction of BC-SNA increased obviously. Despite the difference between D_{va} and
468 physical diameter, such results imply that chemical reactions should be considered as
469 the major pathway for BCOC and BC-SNA particles of ~400 nm D_{va} , while the large-
470 sized BC-aged particles (>1 μ m) may be partially from physical coagulation. The more
471 significant diurnal fluctuations in the OC/ C_n and SNA/ C_n ratios of BCc particles during
472 the ALD period, compared to the LD period, can be attributed to increased primary
473 emissions from resumed society activities, more complex atmospheric chemistry
474 involving reactive gases, and the reinstatement of typical diurnal emission patterns,
475 with higher nighttime RH further enhancing secondary aerosol formation.

476 According to Surdu et al. (2023), condensation involves the direct deposition of gas-
477 phase molecules onto the surface of particles, driven by the difference between the
478 condensable gases concentration (C_g) and its equilibrium particle-phase concentration
479 (C_{eq}), which is negatively affected by RH. In our study, the average RH was relatively
480 high during all three periods (>75%), but the condensable vapor concentration
481 decreased during the lockdown period due to strict lockdown measures, making the
482 difference between C_g and C_{eq} smaller during LD compared to the other two periods.
483 Additionally, we observed a larger mode peak (600 nm, D_{va}) and higher D_{aged}/D_{fresh}
484 ratios (1.11) compared to BLD (510 nm, 1.03) and ALD (500 nm, 1.02) (Figure 6).
485 Therefore, we conclude that condensation was likely inhibited during the LD period.
486 Instead, the conditions likely favored aqueous-phase and heterogeneous reactions,
487 which played a more important role in the evident growth of BCc particles, converting
488 partially coated particles into fully thickly coated BCc during the LD period.

489 Additionally, the larger mode peak (600 nm, D_{va}) and higher D_{aged}/D_{fresh} ratios (1.11)
490 were observed compared to those of BLD (510 nm, 1.03) and ALD (500 nm, 1.02)
491 (Figure 6). Due to the decreased concentrations of the trace reactive gases (e.g., SO₂,
492 NO_x, and VOCs) gases because of the strict lockdown measures and the higher relative
493 humidity (RH > 75%) conditions, which depressed condensing process and facilitate
494 the aqueous or heterogeneous reactions, might play a more important role leading to
495 evident growth in the size of BCc. This aqueous or heterogeneous process during LD
496 likely converted partially coated particles to fully thickly coated BCc as well.

带格式的: 下标

带格式的: 下标

带格式的: 下标

带格式的: 下标

499
500
501

502 3.4 Source apportionment of BCc during lockdown

503 In addition to local emissions, regional transport plays a significant role in influencing
504 pollutant levels. The emergent lockdown in Yangzhou led to strict limitation on local
505 emissions, while surrounding cities were still running as usual. This is supported by
506 **Figure S6**, which illustrates the PM_{2.5} concentrations in Yangzhou and the other five
507 surrounding YRD cities (e.g., Nanjing, Zhenjiang, Changzhou, Taizhou, and Chuzhou)
508 during the campaign. High correlations between PM_{2.5} concentrations in Yangzhou and
509 the other five cities were observed across all different periods (**Figure S6**). These
510 findings underscore the importance of the regional transport in PM_{2.5} pollution during
511 the campaign, providing a unique opportunity to investigate the transmission and source
512 characteristics of BCc in YRD during summer. Herein, PSCF analysis was applied to
513 qualitatively simulate the source probability distributions of the specific BCc particle
514 types (BC-fresh, BC-aged, BCOC, and BC-SNA) during LD.

515
516 As shown in **Figure 10**, the hotspots of potential sources for the four particle types
517 exhibited strong agreements with each other and primarily concentrated in the southeast
518 of Yangzhou, especially along the coast of the Yangtze River, with the WPSCF greater
519 than 0.6. These hotspot areas also encompassed chemical enterprises, power plants,
520 petrochemical industrial parks, and the Yangtze River in the YRD. This evidence
521 suggests that the region of southeast Yangzhou and lower reaches of the Yangtze River
522 are major source areas for the regionally transported BCc in Yangzhou during lockdown.
523 Additionally, Luo et al. (2023) reported that regional transport of pollutants can occur
524 near the surface from upwind areas when the wind speed (WS) exceeds 2 m s⁻¹. **Figure**
525 **S5b** shows that the mean daytime WS was 3 m s⁻¹, indicating that both BC-fresh and
526 BC-aged particles, along with trace gases (e.g., SO₂, NO_x, and VOCs), originating from
527 the hotspot areas, could be transported effectively to Yangzhou. Additionally, the
528 average size of BCc remained around 600 nm at daytime (**Figure S5c**), suggesting that
529 BCc could undergo continual aging reactions under relatively lower RH, but produce
530 relatively thinly coated BCc with smaller sizes than those at nighttime (average size of
531 650 nm). The mean nocturnal WS decreased to 2 m s⁻¹, indicating that the regional
532 atmosphere becomes stagnant (**Figures S5a, b**). As mentioned earlier and underscored
533 here again, this stagnant and humid atmospheric condition may promote aqueous or
534 heterogeneous reactions, likely further leading to the production of more thickly coated
535 BCc than daytime ones.

536

537 4. Conclusions and implications

538 During the summer of 2021, the COVID-19 lockdown imposed in Yangzhou resulted
539 in a significant decrease in anthropogenic emissions from traffic and manufacturing
540 sectors. To examine the effects of this lockdown, we utilized spaceborne observations,

带格式的: 非突出显示

541 ground-based measurements, and particularly SPA-MS analysis to explore the
542 variations, aging characteristics, and sources of BCc in the YRD. We showed that the
543 strict emission controls effectively reduced local gaseous pollutants. However, the
544 decline in NO_x (-39%) and TVOC (-14%) levels might on the other hand result in
545 increased O₃ (28%), leading to a rise in BC-aged particles and a slight elevation in PM_{2.5}
546 levels during the lockdown. Our results revealed a strong non-linear response of PM_{2.5}
547 and O₃ to the gaseous precursors.

548

549 The SPA-MS analysis results further demonstrate significant enhancement of OM and
550 SNA coating species on BC-fresh particles, owing to gas-to-particle partitioning and
551 nocturnal multiphase chemistry. Consequently, we observed a higher fraction of BC-
552 aged particles (73%) during the lockdown due to enhanced oxidizing capacity and high
553 relative humidity (RH > 85%). The BC-fresh particles tended to mix with SNA under
554 high RH conditions, while high TVOC levels were accompanied by BCOC formation.
555 However, BCOC particles generally exhibited smaller sizes compared to BC-SNA
556 particles. Moreover, we propose that aqueous or heterogeneous reactions might be
557 important to generate BCOC and BC-SNA particles, especially ones with 400 nm D_{va},
558 while coagulation might play a more prominent role in larger BC-aged particles. The
559 aging process during LD promoted the conversion of partly coated particles to totally
560 coated ones, with larger diameters (600 nm) and thicker coatings.

561

562 It should be noted that the observed average PM_{2.5} concentration during the lockdown
563 in Yangzhou was 20 μg m⁻³, which still significantly exceeds the WHO's air quality
564 guideline of 5 μg m⁻³. Our research underscores the crucial role of BCc, which
565 constitutes a significant portion of PM_{2.5}, in particulate matter pollution. These particles
566 originate from diverse combustion sources and their behavior is intricately influenced
567 by complex chemistry, regional transport, and meteorological factors. Mere reductions
568 in local primary emissions from traffic and manufacturing sectors exhibit limited
569 efficacy in air quality improvement. Therefore, effective air quality remediation
570 strategies necessitate nuanced control of BCc alongside broader emission reduction
571 efforts. We suggest a more comprehensive regulation of precursor gases from multiple
572 sectors, a wide-ranging joint regulation approach as well as proper consideration of the
573 chemistry, to develop an effective strategy for air quality improvement.

574 **Data availability.** The data in this study are available from the corresponding author
575 upon request (caxinra@163.com).

576

577 **Author contributions.** XG, JW, and YD designed the research. YD, HW, and SC
578 conducted the field measurements. YD, HW, JW, and SC analyzed the data. XG, JW,
579 HL, YW, YZ, and EA reviewed the paper and provided useful suggestions. YD, JW,
580 and XG wrote the first draft of the paper. All people were involved in the discussion of
581 the results.

582

583 **Supplement.** The supplement related to this article is available online at XXX.

584

585 **Competing interests.** The contact author has declared that neither they nor their co-
586 authors have any competing interests.

587

588 **Financial support.** This research has been supported by the National Natural Science
589 Foundation of China (grant nos. 42377100, 22276099, and 42021004).

590 **References**

- 591 Adachi, K., Zaizen, Y., Kajino, M., Igarashi, Y., 2014. Mixing state of regionally
592 transported soot particles and the coating effect on their size and shape at a
593 mountain site in Japan. *Journal of Geophysical Research: Atmospheres* 119,
594 5386–5396. <https://doi.org/10.1002/2013JD020880>
- 595 Benedetti, A., Morcrette, J.-J., Boucher, O., Dethof, A., Engelen, R.J., Fisher, M.,
596 Flentje, H., Huneeus, N., Jones, L., Kaiser, J.W., Kinne, S., Mangold, A.,
597 Razinger, M., Simmons, A.J., Suttie, M., 2009. Aerosol analysis and forecast in
598 the European Centre for Medium-Range Weather Forecasts Integrated Forecast
599 System: 2. Data assimilation. *Journal of Geophysical Research: Atmospheres*
600 114. <https://doi.org/10.1029/2008JD011115>
- 601 Bond, T.C., Bergstrom, R.W., 2006. Light Absorption by Carbonaceous Particles: An
602 Investigative Review. *Aerosol Science and Technology* 40, 27–67.
603 <https://doi.org/10.1080/02786820500421521>
- 604 Bond, T.C., Doherty, S., Fahey, D.W., Forster, P., Berntsen, T., DeAngelo, B., Flanner,
605 M., Ghan, S., Kärcher, B., Koch, D., Kinne, S., Kondo, Y., Quinn, P.K., Sarofim,
606 M., Schultz, M., Michael, S., Venkataraman, C., Zhang, H., Zhang, S., Zender,
607 C.S., 2013. Bounding the role of black carbon in the climate system: A Scientific
608 assessment. *Journal of Geophysical Research: Atmospheres* 118, 5380–5552.
609 <https://doi.org/10.1002/jgrd.50171>
- 610 Cappa, C.D., Zhang, X., Russell, L.M., Collier, S., Lee, A.K.Y., Chen, C.-L., Betha, R.,
611 Chen, S., Liu, J., Price, D.J., Sanchez, K.J., McMeeking, G.R., Williams, L.R.,
612 Onasch, T.B., Worsnop, D.R., Abbatt, J., Zhang, Q., 2019. Light Absorption by
613 Ambient Black and Brown Carbon and its Dependence on Black Carbon
614 Coating State for Two California, USA, Cities in Winter and Summer. *Journal*
615 *of Geophysical Research: Atmospheres* 124, 1550–1577.
616 <https://doi.org/10.1029/2018JD029501>
- 617 Chang, Y., Huang, R., Ge, X., Huang, X., Hu, J., Duan, Y., Zou, Z., Liu, X., Lehmann,
618 M.F., 2020. Puzzling Haze Events in China During the Coronavirus (COVID-
619 19) Shutdown. *Geophys. Res. Lett.* 47. <https://doi.org/10.1029/2020GL088533>
- 620 Chen, H., Huo, J., Fu, Q., Duan, Y., Xiao, H., Chen, J., 2020. Impact of quarantine
621 measures on chemical compositions of PM_{2.5} during the COVID-19 epidemic
622 in Shanghai, China. *Science of The Total Environment* 743, 140758.
623 <https://doi.org/10.1016/j.scitotenv.2020.140758>
- 624 Chen, L., Qi, X., Nie, W., Wang, J., Xu, Zheng, Wang, T., Liu, Y., Shen, Y., Xu,
625 Zhengning, Kokkonen, T., Chi, X., Aalto, P., Paasonen, P., Kerminen, V.-M.,
626 Petäjä, T., Kulmala, M., Ding, A., 2021. Cluster Analysis of Submicron Particle
627 Number Size Distributions at the SORPES Station in the Yangtze River Delta
628 of East China. *Journal of Geophysical Research: Atmospheres* 126.
629 <https://doi.org/10.1029/2020JD034004>
- 630 Chen, L., Zhang, F., Yan, P., Wang, X., Sun, L., Li, Y., Zhang, X., Sun, Y., Li, Z., 2020.
631 The large proportion of black carbon (BC)-containing aerosols in the urban

632 atmosphere. *Environmental Pollution* 263, 114507.
633 <https://doi.org/10.1016/j.envpol.2020.114507>

634 Cheng, Y.F., Su, H., Rose, D., Gunthe, S.S., Berghof, M., Wehner, B., Achtert, P.,
635 Nowak, A., Takegawa, N., Kondo, Y., Shiraiwa, M., Gong, Y.G., Shao, M., Hu,
636 M., Zhu, T., Zhang, Y.H., Carmichael, G.R., Wiedensohler, A., Andreae, M.O.,
637 Pöschl, U., 2012. Size-resolved measurement of the mixing state of soot in the
638 megacity Beijing, China: diurnal cycle, aging and parameterization.
639 *Atmospheric Chemistry and Physics* 12, 4477–4491.
640 <https://doi.org/10.5194/acp-12-4477-2012>

641 Chien, L.-C., Chen, L.-W.A., Lin, R.-T., 2022. Lagged meteorological impacts on
642 COVID-19 incidence among high-risk counties in the United States—a
643 spatiotemporal analysis. *J Expo Sci Environ Epidemiol* 32, 774–781.
644 <https://doi.org/10.1038/s41370-021-00356-y>

645 Clemente, Á., Yubero, E., Nicolás, J.F., Caballero, S., Crespo, J., Galindo, N., 2022.
646 Changes in the concentration and composition of urban aerosols during the
647 COVID-19 lockdown. *Environmental Research* 203, 111788.
648 <https://doi.org/10.1016/j.envres.2021.111788>

649 Cui, S., Xian, J., Shen, F., Zhang, L., Deng, B., Zhang, Y., Ge, X., 2021. One-Year Real-
650 Time Measurement of Black Carbon in the Rural Area of Qingdao, Northeastern
651 China: Seasonal Variations, Meteorological Effects, and the COVID-19 Case
652 Analysis. *Atmosphere* 12, 394. <https://doi.org/10.3390/atmos12030394>

653 Cui, Y., Ji, D., Maenhaut, W., Gao, W., Zhang, R., Wang, Y., 2020. Levels and sources
654 of hourly PM_{2.5}-related elements during the control period of the COVID-19
655 pandemic at a rural site between Beijing and Tianjin. *Science of The Total
656 Environment* 744, 140840. <https://doi.org/10.1016/j.scitotenv.2020.140840>

657 Ding, A., Huang, X., Nie, W., Chi, X., Xu, Zheng, Zheng, L., Xu, Zhengning, Xie, Y.,
658 Qi, X., Shen, Y., Sun, P., Wang, J., Wang, L., Sun, J., Yang, X.-Q., Qin, W.,
659 Zhang, X., Cheng, W., Liu, W., Pan, L., Fu, C., 2019. Significant reduction of
660 PM_{2.5} in eastern China due to regional-scale emission control: evidence from
661 SORPES in 2011–2018. *Atmospheric Chemistry and Physics* 19, 11791–11801.
662 <https://doi.org/10.5194/acp-19-11791-2019>

663 Ding, S., Liu, D., Hu, K., Zhao, D., Tian, P., Wang, F., Li, R., Chen, Y., He, H., Huang,
664 M., Ding, D., 2021. Optical and hygroscopic properties of black carbon
665 influenced by particle microphysics at the top of the anthropogenically polluted
666 boundary layer. *Atmospheric Chemistry & Physics* 21, 681–694.
667 <https://doi.org/10.5194/acp-21-681-2021>

668 Feng, Z., Zheng, F., Liu, Y., Fan, X., Yan, C., Zhang, Y., Daellenbach, K.R., Bianchi, F.,
669 Petäjä, T., Kulmala, M., Bao, X., 2022. Evolution of organic carbon during
670 COVID-19 lockdown period: Possible contribution of nocturnal chemistry. *Sci
671 Total Environ* 808, 152191. <https://doi.org/10.1016/j.scitotenv.2021.152191>

672 Ge, B., Xu, D., Wild, O., Yao, X., Wang, J., Chen, X., Qixin, T., Pan, X., Wang, Z.,
673 2020. Inter-annual variations of wet deposition in Beijing during 2014–2017:

674 implications of below-cloud scavenging of inorganic aerosols.
675 <https://doi.org/10.5194/acp-2020-1146>

676 Gorelick, N., Hancher, M., Dixon, M., Ilyushchenko, S., Thau, D., Moore, R., 2017.
677 Google Earth Engine: Planetary-scale geospatial analysis for everyone. *Remote*
678 *Sensing of Environment, Big Remotely Sensed Data: tools, applications and*
679 *experiences* 202, 18–27. <https://doi.org/10.1016/j.rse.2017.06.031>

680 He, C., Liou, K.-N., Takano, Y., Zhang, R., Levy Zamora, M., Yang, P., Li, Q., Leung,
681 L.R., 2015. Variation of the radiative properties during black carbon aging:
682 theoretical and experimental intercomparison. *Atmospheric Chemistry and*
683 *Physics* 15, 11967–11980. <https://doi.org/10.5194/acp-15-11967-2015>

684 Hopke, P.K., Gao, N., Cheng, M.-D., 1993. Combining chemical and meteorological
685 data to infer source areas of airborne pollutants. *Chemometrics and Intelligent*
686 *Laboratory Systems, Proceedings of the 5th Conference on Computer*
687 *Applications in Analytical Chemistry (COMPANA '92)* 19, 187–199.
688 [https://doi.org/10.1016/0169-7439\(93\)80103-O](https://doi.org/10.1016/0169-7439(93)80103-O)

689 Huang, X., Ding, A., Gao, J., Zheng, B., Zhou, D., Qi, X., Tang, R., Wang, J., Ren, C.,
690 Nie, W., Chi, X., Xu, Z., Chen, L., Li, Y., Che, F., Pang, N., Wang, H., Tong, D.,
691 Qin, W., Cheng, W., Liu, W., Fu, Q., Liu, B., Chai, F., Davis, S.J., Zhang, Q.,
692 He, K., 2021. Enhanced secondary pollution offset reduction of primary
693 emissions during COVID-19 lockdown in China. *Natl Sci Rev* 8, nwaal37.
694 <https://doi.org/10.1093/nsr/nwaal37>

695 Huang, X., Wang, Z., Ding, A., 2018. Impact of Aerosol-PBL Interaction on Haze
696 Pollution: Multiyear Observational Evidences in North China. *Geophysical*
697 *Research Letters* 45, 8596–8603. <https://doi.org/10.1029/2018GL079239>

698 Isokääntä, S., Kim, P., Mikkonen, S., Kühn, T., Kokkola, H., Yli-Juuti, T., Heikkinen,
699 L., Luoma, K., Petäjä, T., Kipling, Z., Partridge, D., Virtanen, A., 2022. The
700 effect of clouds and precipitation on the aerosol concentrations and composition
701 in a boreal forest environment. *Atmospheric Chemistry and Physics* 22, 11823–
702 11843. <https://doi.org/10.5194/acp-22-11823-2022>

703 Jacobson, M.Z., 2002. Analysis of aerosol interactions with numerical techniques for
704 solving coagulation, nucleation, condensation, dissolution, and reversible
705 chemistry among multiple size distributions. *Journal of Geophysical Research:*
706 *Atmospheres* 107, AAC 2-1-AAC 2-23. <https://doi.org/10.1029/2001JD002044>

707 Jain, C.D., Madhavan, B.L., Singh, V., Prasad, P., Sai Krishnaveni, A., Ravi Kiran, V.,
708 Venkat Ratnam, M., 2021. Phase-wise analysis of the COVID-19 lockdown
709 impact on aerosol, radiation and trace gases and associated chemistry in a
710 tropical rural environment. *Environmental Research* 194, 110665.
711 <https://doi.org/10.1016/j.envres.2020.110665>

712 Jeong, C.-H., Yousif, M., Evans, G.J., 2022. Impact of the COVID-19 lockdown on the
713 chemical composition and sources of urban PM_{2.5}. *Environmental Pollution*
714 292, 118417. <https://doi.org/10.1016/j.envpol.2021.118417>

715 Kahnert, M., 2010. On the Discrepancy between Modeled and Measured Mass

716 Absorption Cross Sections of Light Absorbing Carbon Aerosols. *Aerosol*
717 *Science and Technology* 44, 453–460.
718 <https://doi.org/10.1080/02786821003733834>

719 Kandler, K., Schneiders, K., Ebert, M., Hartmann, M., Weinbruch, S., Prass, M.,
720 Pöhlker, C., 2018. Composition and mixing state of atmospheric aerosols
721 determined by electron microscopy: method development and application to
722 aged Saharan dust deposition in the Caribbean boundary layer. *Atmospheric*
723 *Chemistry and Physics* 18, 13429–13455. [https://doi.org/10.5194/acp-18-](https://doi.org/10.5194/acp-18-13429-2018)
724 [13429-2018](https://doi.org/10.5194/acp-18-13429-2018)

725 Kondo, Y., Matsui, H., Moteki, N., Sahu, L., Takegawa, N., Kajino, M., Zhao, Y.,
726 Cubison, M.J., Jimenez, J.L., Vay, S., Diskin, G.S., Anderson, B., Wisthaler, A.,
727 Mikoviny, T., Fuelberg, H.E., Blake, D.R., Huey, G., Weinheimer, A.J., Knapp,
728 D.J., Brune, W.H., 2011. Emissions of black carbon, organic, and inorganic
729 aerosols from biomass burning in North America and Asia in 2008. *Journal of*
730 *Geophysical Research: Atmospheres* 116.
731 <https://doi.org/10.1029/2010JD015152>

732 Laughner, J.L., Neu, J.L., Schimel, D., Wennberg, P.O., Barsanti, K., Bowman, K.W.,
733 Chatterjee, A., Croes, B.E., Fitzmaurice, H.L., Henze, D.K., Kim, J., Kort, E.A.,
734 Liu, Z., Miyazaki, K., Turner, A.J., Anenberg, S., Avise, J., Cao, H., Crisp, D.,
735 de Gouw, J., Eldering, A., Fyfe, J.C., Goldberg, D.L., Gurney, K.R.,
736 Hasheminassab, S., Hopkins, F., Ivey, C.E., Jones, D.B.A., Liu, J., Lovenduski,
737 N.S., Martin, R.V., McKinley, G.A., Ott, L., Poulter, B., Ru, M., Sander, S.P.,
738 Swart, N., Yung, Y.L., Zeng, Z.-C., 2021. Societal shifts due to COVID-19
739 reveal large-scale complexities and feedbacks between atmospheric chemistry
740 and climate change. *Proc Natl Acad Sci U S A* 118, e2109481118.
741 <https://doi.org/10.1073/pnas.2109481118>

742 Le, T., Wang, Y., Liu, L., Yang, J., Yung, Y.L., Li, G., Seinfeld, J.H., 2020. Unexpected
743 air pollution with marked emission reductions during the COVID-19 outbreak
744 in China. *Science* 369, 702–706. <https://doi.org/10.1126/science.abb7431>

745 Li, J., Jiang, L., Chen, C., Liu, D., Du, S., Zhang, Y., Yang, Y., Tang, L., 2020.
746 Characteristics and Sources of Black Carbon Aerosol in a Mega-City in the
747 Western Yangtze River Delta, China. *Atmosphere* 11, 315.
748 <https://doi.org/10.3390/atmos11040315>

749 Li, K., Wang, X., Lu, X., Chen, H., Yang, X., 2022. Effects of Volatile Components on
750 Mixing State and Size Distribution of Individual Black Carbon Aerosols.
751 *Aerosol Air Qual. Res.* 22, 210400. <https://doi.org/10.4209/aaqr.210400>

752 Li, L., Huang, Z., Dong, J., Li, M., Gao, W., Nian, H., Fu, Z., Zhang, G., Bi, X., Cheng,
753 P., Zhou, Z., 2011. Real time bipolar time-of-flight mass spectrometer for
754 analyzing single aerosol particles. *International Journal of Mass Spectrometry*
755 303, 118–124. <https://doi.org/10.1016/j.ijms.2011.01.017>

756 Li, L., Li, Q., Huang, L., Wang, Q., Zhu, A., Xu, J., Liu, Ziyi, Li, H., Shi, L., Li, R.,
757 Azari, M., Wang, Y., Zhang, X., Liu, Zhiqiang, Zhu, Y., Zhang, K., Xue, S., Ooi,

758 M.C.G., Zhang, D., Chan, A., 2020. Air quality changes during the COVID-19
759 lockdown over the Yangtze River Delta Region: An insight into the impact of
760 human activity pattern changes on air pollution variation. *Science of The Total*
761 *Environment* 732, 139282. <https://doi.org/10.1016/j.scitotenv.2020.139282>

762 Liu, D., Joshi, R., Wang, J., Yu, C., Allan, J.D., Coe, H., Flynn, M.J., Xie, C., Lee, J.,
763 Squires, F., Kotthaus, S., Grimmond, S., Ge, X., Sun, Y., Fu, P., 2019.
764 Contrasting physical properties of black carbon in urban Beijing between winter
765 and summer. *Atmospheric Chemistry and Physics* 19, 6749–6769.
766 <https://doi.org/10.5194/acp-19-6749-2019>

767 Liu, Q., Jing, B., Peng, C., Tong, S., Wang, W., Ge, M., 2016. Hygroscopicity of
768 internally mixed multi-component aerosol particles of atmospheric relevance.
769 *Atmospheric Environment* 125, 69–77.
770 <https://doi.org/10.1016/j.atmosenv.2015.11.003>

771 Luo, J., Li, Z., Zhang, C., Zhang, Q., Zhang, Yongming, Zhang, Ying, Curci, G.,
772 Chakrabarty, R.K., 2022. Regional impacts of black carbon morphologies on
773 shortwave aerosol–radiation interactions: a comparative study between the US
774 and China. *Atmospheric Chemistry and Physics* 22, 7647–7666.
775 <https://doi.org/10.5194/acp-22-7647-2022>

776 Moffet, R.C., Rödel, T.C., Kelly, S.T., Yu, X.Y., Carroll, G.T., Fast, J., Zaveri, R.A.,
777 Laskin, A., Gilles, M.K., 2013. Spectro-microscopic measurements of
778 carbonaceous aerosol aging in Central California. *Atmospheric Chemistry and*
779 *Physics* 13, 10445–10459. <https://doi.org/10.5194/acp-13-10445-2013>

780 Morcrette, J.-J., Boucher, O., Jones, L., Salmond, D., Bechtold, P., Beljaars, A.,
781 Benedetti, A., Bonet, A., Kaiser, J.W., Razinger, M., Schulz, M., Serrar, S.,
782 Simmons, A.J., Sofiev, M., Suttie, M., Tompkins, A.M., Untch, A., 2009.
783 Aerosol analysis and forecast in the European Centre for Medium-Range
784 Weather Forecasts Integrated Forecast System: Forward modeling. *Journal of*
785 *Geophysical Research: Atmospheres* 114.
786 <https://doi.org/10.1029/2008JD011235>

787 Nie, D., Shen, F., Wang, J., Ma, X., Li, Z., Ge, P., Ou, Y., Jiang, Y., Chen, Meijuan,
788 Chen, Mindong, Wang, T., Ge, X., 2021. Changes of air quality and its
789 associated health and economic burden in 31 provincial capital cities in China
790 during COVID-19 pandemic. *Atmos Res* 249, 105328.
791 <https://doi.org/10.1016/j.atmosres.2020.105328>

792 Peng, J., Hu, M., Guo, S., Du, Z., Zheng, Jing, Shang, D., Levy Zamora, M., Zeng, L.,
793 Shao, M., Wu, Y.-S., Zheng, Jun, Wang, Y., Glen, C.R., Collins, D.R., Molina,
794 M.J., Zhang, R., 2016. Markedly enhanced absorption and direct radiative
795 forcing of black carbon under polluted urban environments. *Proceedings of the*
796 *National Academy of Sciences* 113, 4266–4271.
797 <https://doi.org/10.1073/pnas.1602310113>

798 Polissar, A.V., Hopke, P.K., Paatero, P., Kaufmann, Y.J., Hall, D.K., Bodhaine, B.A.,
799 Dutton, E.G., Harris, J.M., 1999. The aerosol at Barrow, Alaska: long-term

800 trends and source locations. *Atmospheric Environment* 33, 2441–2458.
801 [https://doi.org/10.1016/S1352-2310\(98\)00423-3](https://doi.org/10.1016/S1352-2310(98)00423-3)

802 Qin, M., Hu, A., Mao, J., Li, X., Sheng, L., Sun, J., Li, J., Wang, X., Zhang, Y., Hu, J.,
803 2021. PM_{2.5} and O₃ relationships affected by the atmospheric oxidizing
804 capacity in the Yangtze River Delta, China. *Science of The Total Environment*
805 152268. <https://doi.org/10.1016/j.scitotenv.2021.152268>

806 Ramanathan, V., Carmichael, G., 2008. Global and regional climate changes due to
807 black carbon. *Nature Geoscience* 1, 221–227. <https://doi.org/10.1038/ngeo156>

808 Sedlacek, A.J., Lewis, E.R., Onasch, T.B., Zuidema, P., Redemann, J., Jaffe, D.,
809 Kleinman, L.I., 2022. Using the Black Carbon Particle Mixing State to
810 Characterize the Lifecycle of Biomass Burning Aerosols. *Environ. Sci. Technol.*
811 56, 14315–14325. <https://doi.org/10.1021/acs.est.2c03851>

812 Silva, P.J., Liu, D.-Y., Noble, C.A., Prather, K.A., 1999. Size and Chemical
813 Characterization of Individual Particles Resulting from Biomass Burning of
814 Local Southern California Species. *Environ. Sci. Technol.* 33, 3068–3076.
815 <https://doi.org/10.1021/es980544p>

816 Song, X.-H., Hopke, P.K., Fergenson, D.P., Prather, K.A., 1999. Classification of Single
817 Particles Analyzed by ATOFMS Using an Artificial Neural Network, ART-2A.
818 *Anal. Chem.* 71, 860–865. <https://doi.org/10.1021/ac9809682>

819 Steinfeld, J.I., 1998. Atmospheric Chemistry and Physics: From Air Pollution to
820 Climate Change. *Environment: Science and Policy for Sustainable*
821 *Development* 40, 26–26. <https://doi.org/10.1080/00139157.1999.10544295>

822 Sulaymon, I.D., Zhang, Yuanxun, Hopke, P.K., Hu, J., Zhang, Yang, Li, L., Mei, X.,
823 Gong, K., Shi, Z., Zhao, B., Zhao, F., 2021a. Persistent high PM_{2.5} pollution
824 driven by unfavorable meteorological conditions during the COVID-19
825 lockdown period in the Beijing-Tianjin-Hebei region, China. *Environmental*
826 *Research* 198, 111186. <https://doi.org/10.1016/j.envres.2021.111186>

827 Sulaymon, I.D., Zhang, Yuanxun, Hopke, P.K., Zhang, Yang, Hua, J., Mei, X., 2021b.
828 COVID-19 pandemic in Wuhan: Ambient air quality and the relationships
829 between criteria air pollutants and meteorological variables before, during, and
830 after lockdown. *Atmospheric Research* 250, 105362.
831 <https://doi.org/10.1016/j.atmosres.2020.105362>

832 Sun, J., Sun, Y., Xie, C., Xu, Weiqi, Chen, C., Wang, Zhe, Li, L., Du, X., Huang, F., Li,
833 Y., Li, Z., Pan, X., Ma, N., Xu, Wanyun, Fu, P., Wang, Zifa, 2022. The chemical
834 composition and mixing state of BC-containing particles and the implications
835 on light absorption enhancement. *Atmos. Chem. Phys.* 22, 7619–7630.
836 <https://doi.org/10.5194/acp-22-7619-2022>

837 Sun, J., Wang, Zhe, Zhou, W., Xie, C., Wu, C., Chen, C., Han, T., Wang, Q., Li, Z., Li,
838 J., Fu, P., Wang, Zifa, Sun, Y., 2021. Measurement report: Long-term changes
839 in black carbon and aerosol optical properties from 2012 to 2020 in Beijing,
840 China (preprint). *Aerosols/Field Measurements/Troposphere/Physics (physical*
841 *properties and processes)*. <https://doi.org/10.5194/acp-2021-637>

842 Sun, Y., Du, W., Fu, P., Wang, Q., Li, J., Ge, X., Zhang, Q., Zhu, C., Ren, L., Xu, W.,
843 Zhao, J., Han, T., Worsnop, D.R., Wang, Z., 2016. Primary and secondary
844 aerosols in Beijing in winter: sources, variations and processes. *Atmos. Chem.*
845 *Phys.*

846 Sun, Y., Lei, L., Zhou, W., Chen, C., He, Y., Sun, J., Li, Z., Xu, W., Wang, Q., Ji, D., Fu,
847 P., Wang, Z., Worsnop, D.R., 2020. A chemical cocktail during the COVID-19
848 outbreak in Beijing, China: Insights from six-year aerosol particle composition
849 measurements during the Chinese New Year holiday. *Science of The Total*
850 *Environment* 742, 140739. <https://doi.org/10.1016/j.scitotenv.2020.140739>

851 Surdu, M., Lamkaddam, H., Wang, D.S., Bell, D.M., Xiao, M., Lee, C.P., Li, D.,
852 Caudillo, L., Marie, G., Scholz, W., Wang, M., Lopez, B., Piedehierro, A.A.,
853 Ataei, F., Baalbaki, R., Bertozzi, B., Bogert, P., Brasseur, Z., Dada, L., Duplissy,
854 J., Finkenzeller, H., He, X.-C., Höhler, K., Korhonen, K., Krechmer, J.E.,
855 Lehtipalo, K., Mahfouz, N.G.A., Manninen, H.E., Marten, R., Massabò, D.,
856 Mauldin, R., Petäjä, T., Pfeifer, J., Philippov, M., Rörup, B., Simon, M., Shen,
857 J., Umo, N.S., Vogel, F., Weber, S.K., Zauner-Wieczorek, M., Volkamer, R.,
858 Saathoff, H., Möhler, O., Kirkby, J., Worsnop, D.R., Kulmala, M., Stratmann,
859 F., Hansel, A., Curtius, J., Welti, A., Riva, M., Donahue, N.M., Baltensperger,
860 U., El Haddad, I., 2023. Molecular Understanding of the Enhancement in
861 Organic Aerosol Mass at High Relative Humidity. *Environ Sci Technol* 57,
862 2297–2309. <https://doi.org/10.1021/acs.est.2c04587>

863 Taylor, J.W., Allan, J.D., Allen, G., Coe, H., Williams, P.I., Flynn, M.J., Le Breton, M.,
864 Muller, J.B.A., Percival, C.J., Oram, D., Forster, G., Lee, J.D., Rickard, A.R.,
865 Parrington, M., Palmer, P.I., 2014. Size-dependent wet removal of black carbon
866 in Canadian biomass burning plumes. *Atmospheric Chemistry and Physics* 14,
867 13755–13771. <https://doi.org/10.5194/acp-14-13755-2014>

868 Wang, H., Miao, Q., Shen, L., Yang, Q., Wu, Y., Wei, H., 2021. Air pollutant variations
869 in Suzhou during the 2019 novel coronavirus (COVID-19) lockdown of 2020:
870 High time-resolution measurements of aerosol chemical compositions and
871 source apportionment. *Environmental Pollution* 271, 116298.
872 <https://doi.org/10.1016/j.envpol.2020.116298>

873 Wang, J., Ge, X., Sonya, C., Ye, J., Lei, Y., Chen, M., Zhang, Q., 2022. Influence of
874 regional emission controls on the chemical composition, sources, and size
875 distributions of submicron aerosols: Insights from the 2014 Nanjing Youth
876 Olympic Games. *Science of The Total Environment* 807, 150869.
877 <https://doi.org/10.1016/j.scitotenv.2021.150869>

878 Wang, J., Liu, D., Ge, X., Wu, Y., Shen, F., Chen, M., Zhao, J., Xie, C., Wang, Q., Xu,
879 W., Zhang, J., Hu, J., Allan, J., Joshi, R., Fu, P., Coe, H., Sun, Y., 2019.
880 Characterization of black carbon-containing fine particles in Beijing during
881 wintertime. *Atmos. Chem. Phys.* 19, 447–458. [https://doi.org/10.5194/acp-19-](https://doi.org/10.5194/acp-19-447-2019)
882 [447-2019](https://doi.org/10.5194/acp-19-447-2019)

883 Wang, Pengfei, Chen, K., Zhu, S., Wang, Peng, Zhang, H., 2020. Severe air pollution

884 events not avoided by reduced anthropogenic activities during COVID-19
885 outbreak. *Resources, Conservation and Recycling* 158, 104814.
886 <https://doi.org/10.1016/j.resconrec.2020.104814>

887 Wang, Q., Liu, S., Zhou, Y., Cao, J., Han, Y., Ni, H., Zhang, N., Huang, R., 2015.
888 Characteristics of Black Carbon Aerosol during the Chinese Lunar Year and
889 Weekdays in Xi'an, China. *Atmosphere* 6, 195–208.
890 <https://doi.org/10.3390/atmos6020195>

891 Wang, S., Zhao, M., Xing, J., Wu, Y., Zhou, Y., Lei, Y., He, K., Fu, L., Hao, J., 2010.
892 Quantifying the Air Pollutants Emission Reduction during the 2008 Olympic
893 Games in Beijing. *Environ. Sci. Technol.* 44, 2490–2496.
894 <https://doi.org/10.1021/es9028167>

895 Wang, Y., Zhu, S., Ma, J., Shen, J., Wang, Pengfei, Wang, Peng, Zhang, H., 2021.
896 Enhanced atmospheric oxidation capacity and associated ozone increases
897 during COVID-19 lockdown in the Yangtze River Delta. *Science of The Total*
898 *Environment* 768, 144796. <https://doi.org/10.1016/j.scitotenv.2020.144796>

899 Wang, Y.Q., 2014. MeteoInfo: GIS software for meteorological data visualization and
900 analysis. *Meteorological Applications* 21, 360–368.
901 <https://doi.org/10.1002/met.1345>

902 Wang, Y.Q., Zhang, X.Y., Draxler, R.R., 2009. TrajStat: GIS-based software that uses
903 various trajectory statistical analysis methods to identify potential sources from
904 long-term air pollution measurement data. *Environmental Modelling &*
905 *Software* 24, 938–939. <https://doi.org/10.1016/j.envsoft.2009.01.004>

906 WHO global air quality guidelines: Particulate matter (PM_{2.5} and PM₁₀), ozone,
907 nitrogen dioxide, sulfur dioxide and carbon monoxide, 2021. , WHO Guidelines
908 Approved by the Guidelines Review Committee. World Health Organization,
909 Geneva.

910 Xie, C., He, Y., Lei, L., Zhou, W., Liu, J., Wang, Q., Xu, W., Qiu, Y., Zhao, J., Sun, J.,
911 Li, L., Li, M., Zhou, Z., Fu, P., Wang, Z., Sun, Y., 2020. Contrasting mixing
912 state of black carbon-containing particles in summer and winter in Beijing.
913 *Environmental Pollution* 263, 114455.
914 <https://doi.org/10.1016/j.envpol.2020.114455>

915 Xu, J., Ge, X., Zhang, X., Zhao, W., Zhang, R., Zhang, Y., 2020. COVID-19 Impact on
916 the Concentration and Composition of Submicron Particulate Matter in a
917 Typical City of Northwest China. *Geophysical Research Letters* 47,
918 e2020GL089035. <https://doi.org/10.1029/2020GL089035>

919 Yang, J., Ma, S., Gao, B., Li, X., Zhang, Y., Cai, J., Li, M., Yao, L., Huang, B., Zheng,
920 M., 2017. Single particle mass spectral signatures from vehicle exhaust particles
921 and the source apportionment of on-line PM_{2.5} by single particle aerosol mass
922 spectrometry. *Science of The Total Environment* 593–594, 310–318.
923 <https://doi.org/10.1016/j.scitotenv.2017.03.099>

924 Zhang, G., Fu, Y., Peng, X., Sun, W., Shi, Z., Song, W., Hu, W., Chen, D., Lian, X., Li,
925 L., Tang, M., Wang, X., Bi, X., 2021. Black Carbon Involved Photochemistry

926 Enhances the Formation of Sulfate in the Ambient Atmosphere: Evidence From
927 In Situ Individual Particle Investigation. *Geophys Res Atmos* 126.
928 <https://doi.org/10.1029/2021JD035226>

929 Zhang, J., Li, H., Chen, L., Huang, X., Zhang, W., Zhao, R., 2022. Particle composition,
930 sources and evolution during the COVID-19 lockdown period in Chengdu,
931 southwest China: Insights from single particle aerosol mass spectrometer data.
932 *Atmospheric Environment* 268, 118844.
933 <https://doi.org/10.1016/j.atmosenv.2021.118844>

934 Zhang, J., Yuan, Q., Liu, L., Wang, Y., Zhang, Y., Xu, L., Pang, Y., Zhu, Y., Niu, H.,
935 Shao, L., Yang, S., Liu, H., Pan, X., Shi, Z., Hu, M., Fu, P., Li, W., 2021. Trans-
936 Regional Transport of Haze Particles From the North China Plain to Yangtze
937 River Delta During Winter. *JGR Atmospheres* 126.
938 <https://doi.org/10.1029/2020JD033778>

939 Zhang, K., Liu, Z., Zhang, X., Li, Q., Jensen, A., Tan, W., Huang, L., Wang, Y., de Gouw,
940 J., Li, L., 2022. Insights into the significant increase in ozone during COVID-
941 19 in a typical urban city of China. *Atmos. Chem. Phys.* 22, 4853–4866.
942 <https://doi.org/10.5194/acp-22-4853-2022>

943 Zhang, Y., Liu, X., Zhang, L., Tang, A., Goulding, K., Collett, J.L., 2021. Evolution of
944 secondary inorganic aerosols amidst improving PM2.5 air quality in the North
945 China plain. *Environmental Pollution* 281, 117027.
946 <https://doi.org/10.1016/j.envpol.2021.117027>

947 Zhang Y., Wang X., Chen H., Yang X., Chen J., Alien J.O., 2009. Source Apportionment
948 Of Lead-containing Aerosol Particles In Shanghai Using Single Particle Mass
949 Spectrometry. *Chemosphere* 74, 501–507.

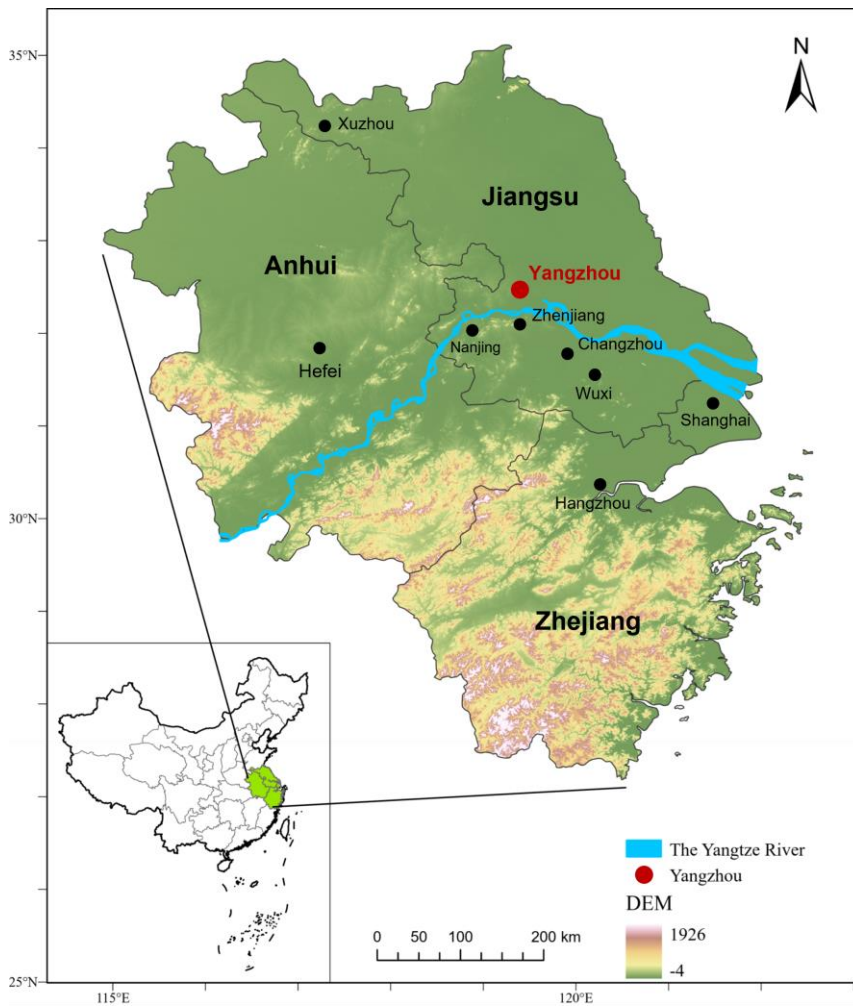
950 Zhang, Y., Yuan, Q., Huang, D., Kong, S., Zhang, J., Wang, X., Lu, C., Shi, Z., Zhang,
951 X., Sun, Y., Wang, Z., Shao, L., Zhu, J., Li, W., 2018. Direct Observations of
952 Fine Primary Particles From Residential Coal Burning: Insights Into Their
953 Morphology, Composition, and Hygroscopicity. *Journal of Geophysical*
954 *Research: Atmospheres* 123, 12,964-12,979.
955 <https://doi.org/10.1029/2018JD028988>

956 Zhang, Z., Li, H., Ho, W., Cui, L., Men, Q., Cao, L., Zhang, Y., Wang, J., Huang, C.,
957 Lee, S., Huang, Y., Chen, M., Ge, X., 2024. Critical Roles of Surface-Enhanced
958 Heterogeneous Oxidation of SO₂ in Haze Chemistry: Review of Extended
959 Pathways for Complex Air Pollution. *Curr Pollution Rep.*
960 <https://doi.org/10.1007/s40726-023-00287-2>

961 Zhou, H., Liu, T., Sun, B., Tian, Y., Zhou, X., Hao, F., Chun, X., Wan, Z., Liu, P., Wang,
962 J., Du, D., 2022. Chemical characteristics and sources of PM_{2.5} in Hohhot, a
963 semi-arid city in northern China: insight from the COVID-19 lockdown. *Atmos.*
964 *Chem. Phys.* 14.

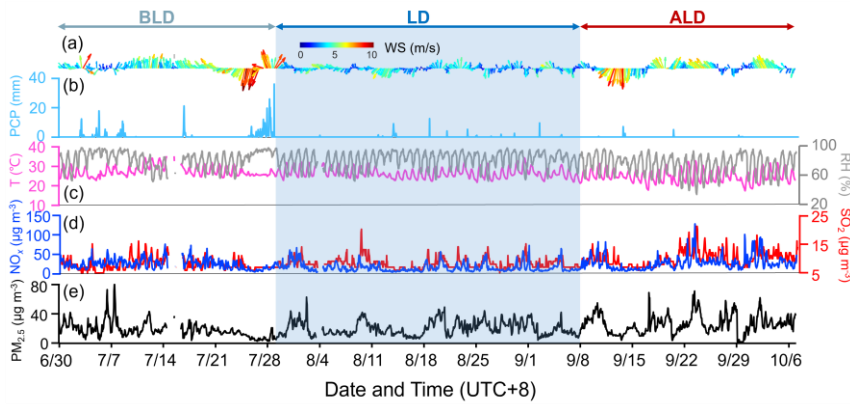
965 Zhou, X., Gao, J., Wang, T., Wu, W., Wang, W., 2009. Measurement of black carbon
966 aerosols near two Chinese megacities and the implications for improving
967 emission inventories. *Atmospheric Environment* 43, 3918–3924.

968 <https://doi.org/10.1016/j.atmosenv.2009.04.062>
969 Zhou, Y., Wu, Y., Yang, L., Fu, L., He, K., Wang, S., Hao, J., Chen, J., Li, C., 2010. The
970 impact of transportation control measures on emission reductions during the
971 2008 Olympic Games in Beijing, China. *Atmospheric Environment* 44, 285–
972 293. <https://doi.org/10.1016/j.atmosenv.2009.10.040>
973 Zhu, X., Hu, B., Xin, J., Wang, L., Münkel, C., Mao, G., Wang, Y., 2015. Impact of
974 emission controls on air quality in Beijing during APEC 2014: Lidar ceilometer
975 observations. *ATMOSPHERIC CHEMISTRY AND PHYSICS* 15, 12667–
976 12680. <https://doi.org/10.5194/acp-15-12667-2015>
977
978



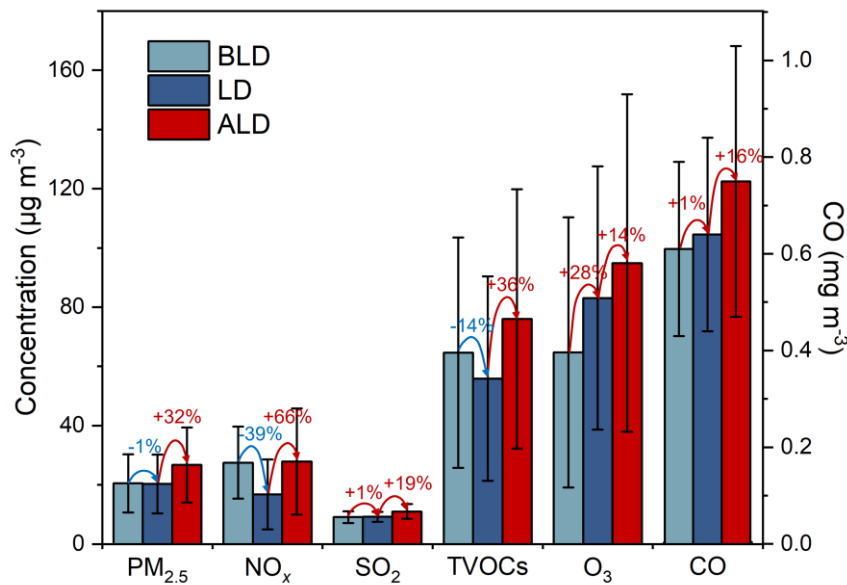
979 **Figure 1.** Geographical overview of the Yangtze River Delta (YRD) Region in China,
980

981 depicting the major cities within the YRD and the sampling site located in Yangzhou.
 982 The color gradient from green to white indicates varying altitudes across the region
 983 (Maps were generated by using ArcGIS Pro).



984

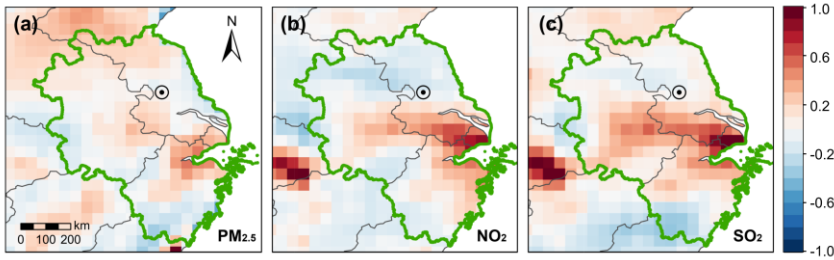
985 **Figure 2.** Temporal variations of (a) wind direction (WD) and wind speed (WS), (b)
 986 precipitation (PCP), (c) temperature (T) and relative humidity (RH), (d) concentrations
 987 of NO_x and SO₂, and (e) mass loading of PM_{2.5}. The grey, blue, and red arrow ranges
 988 denote the periods before lockdown (BLD), during lockdown (LD), and after lockdown
 989 (ALD).



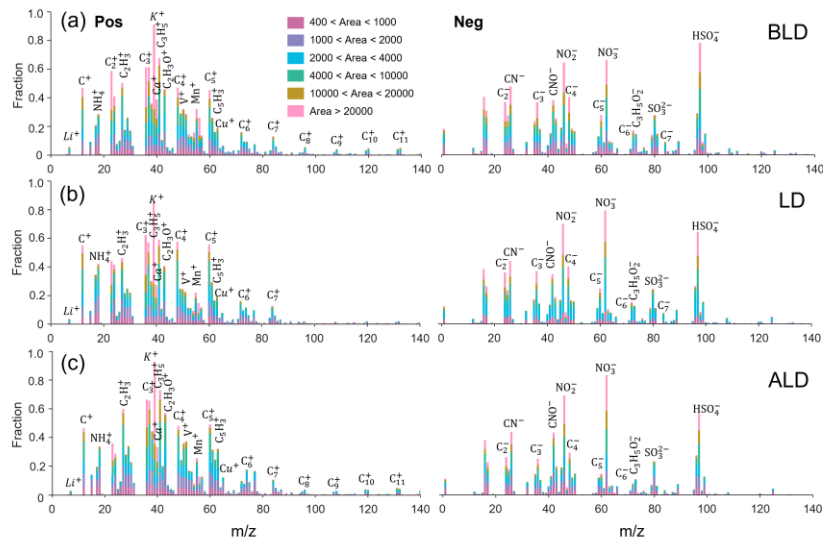
990

991 **Figure 3.** Ground-based observations of PM_{2.5}, NO_x, SO₂, O₃, CO, and TVOC

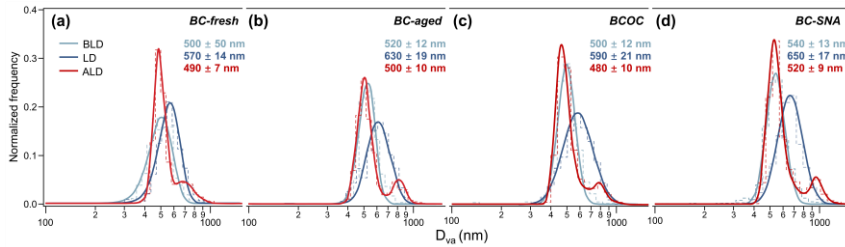
992 concentrations in Yangzhou. The figure compares the averages during the BLD (grey),
 993 LD (blue), and ALD (red) periods. Error bars indicate SDs over different lockdown
 994 periods.
 995



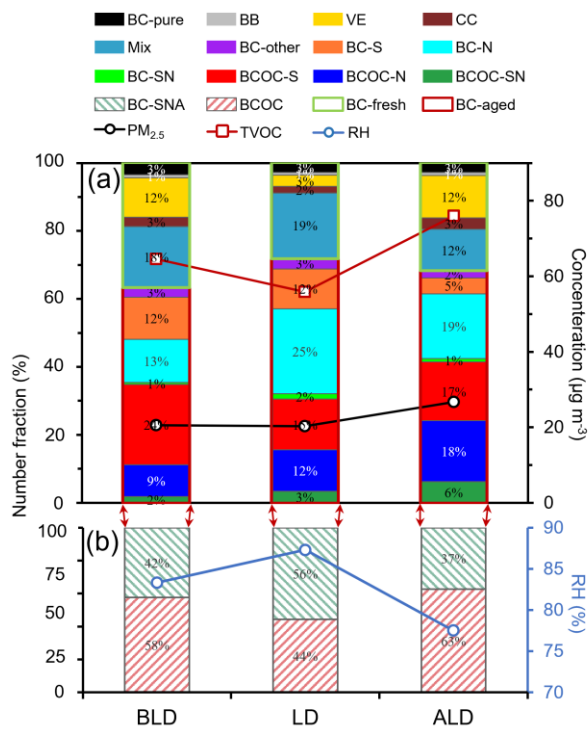
996
 997 **Figure 4.** The fractional changes (i.e., $(LD - BLD)/BLD$) of (a) $PM_{2.5}$, (b) NO_2 , and (c)
 998 SO_2 between BLD and LD periods based on spaceborne measurement. The circle
 999 symbols in the maps indicate the location of Yangzhou, and the green region represents
 1000 the YRD.



1001
 1002 **Figure 5.** The average positive and negative mass spectra of BCc (a) before the
 1003 lockdown period (BLD), (b) during the lockdown period (LD), and (c)
 1004 after the lockdown period (ALD).
 1005

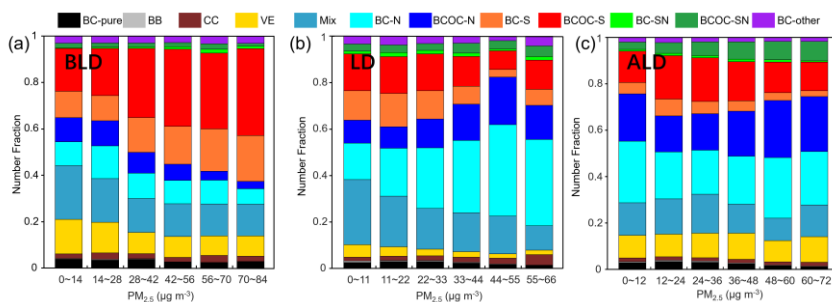


1006
 1007 **Figure 6.** Size distribution of different types of BCc during different periods in
 1008 Yangzhou. **(a)** BC-fresh particles, **(b)** BC-aged particles, **(c)** BCOC particles, and **(d)**
 1009 BC-SNA particles. The Log-normal distribution was used to fit the unimodal size
 1010 distribution, and the Lorentz distribution was used to fit the bimodal size
 1011 distribution. The corresponding mode sizes (with the standard deviations) are also shown.
 1012

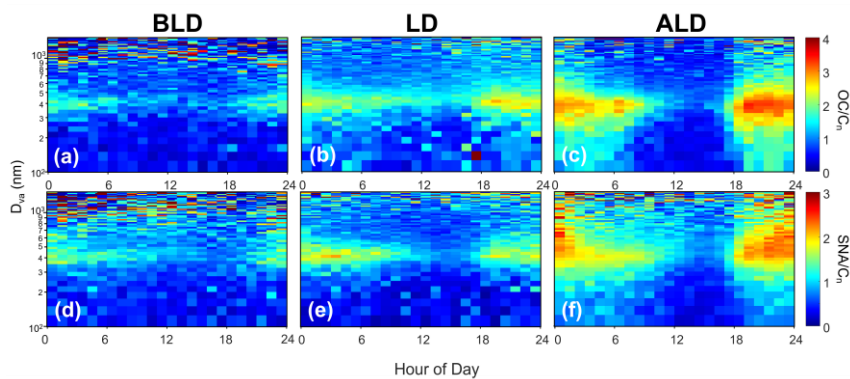


1013
 1014 **Figure 7.** Number fractions of BCc. **(a)** The number fractions of different BCc along
 1015 with the concentrations of PM_{2.5} and total volatile organic compounds (TVOC). **(b)** The

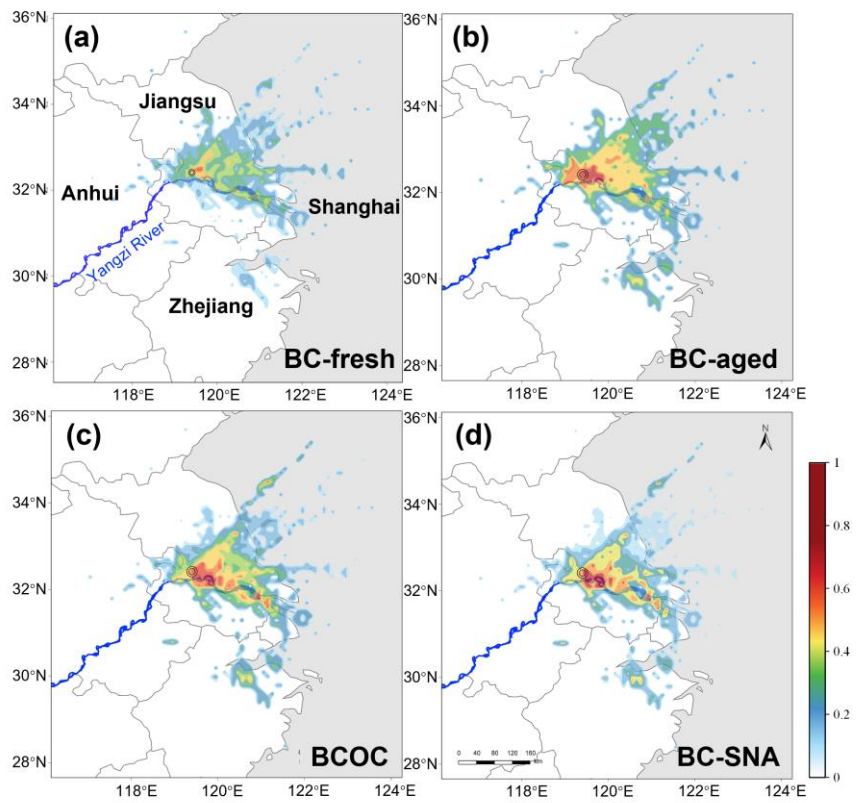
1016 number fractions of different types of BC-aged particles along with relative humidity
 1017 (RH).
 1018



1019
 1020 **Figure 8.** Variations of number fractions of BCc particle types with PM_{2.5} mass
 1021 concentrations during (a) the BLD period, (b) LD, and (c) the ALD period.



1022
 1023 **Figure 9.** Diurnal variations of the ratios of OC/C_n and SNA/C_n with a size distribution
 1024 of BCc during (a, d) BLD, (b, e) LD, and (c, f) ALD.



1025

1026 **Figure 10.** The PSCF maps for different BCc during LD. (a) BC-fresh. (b) BC-aged.

1027 (c) BCOC. (d) BC-SNA.

1028